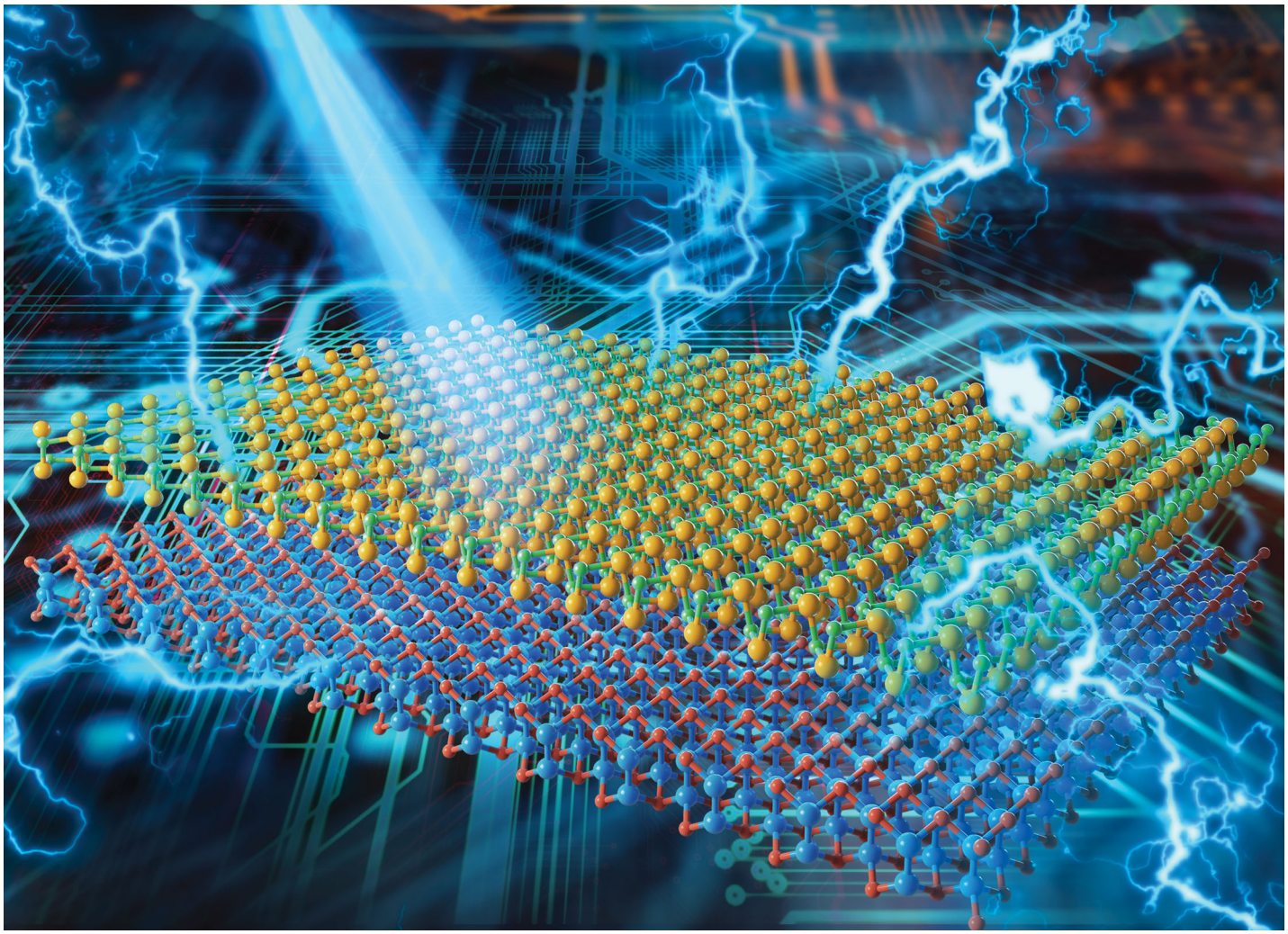

**Showcasing collaborative research from East China Normal University, Shanxi University and Fudan University, China**

A type-II GaSe/GeS heterobilayer with strain enhanced photovoltaic properties and external electric field effects

2D GaSe/GeS van der Waals heterostructures with robust type-II band alignment, tunable band offset and strain enhanced photovoltaic effect will have great application prospects in future photovoltaic and optoelectric nanodevices.

## As featured in:

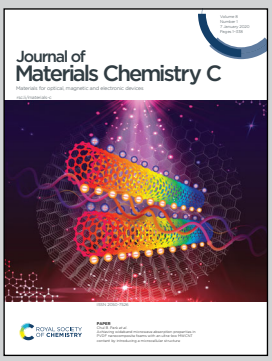


See Shi-Jing Gong, Zhigao Hu *et al.*, *J. Mater. Chem. C*, 2020, **8**, 89.

ROYAL SOCIETY OF CHEMISTRY

rsc.li/materials-c

Registered charity number: 207890

Journal of Materials Chemistry C

PAPER

View Article Online
View Journal | View Issue



Cite this: J. Mater. Chem. C, 2020, 8, 89

# A type-II GaSe/GeS heterobilayer with strain enhanced photovoltaic properties and external electric field effects†

Bin Zhou,[a] Shi-Jing Gong,*[b] Kai Jiang,[a] Liping Xu,[a] Liyan Shang,[a] Jinzhong Zhang,[a] Zhigao Hu*[acd] and Junhao Chu[acd]

Received 25th October 2019,
Accepted 29th October 2019

DOI: 10.1039/c9tc05840k

rsc.li/materials-c

Constructing two dimensional (2D) van der Waals (vdW) heterostructures and understanding their electronic properties are pivotal for developing novel electronic devices. In this work, by using the first-principles calculations, we theoretically demonstrate that the 2D GaSe/GeS van der Waals (vdW) heterobilayer is a robust type-II band alignment semiconductor with a direct band gap of 1.8 eV. It exhibits a remarkable absorbance coefficient of $\sim 10^5$ cm$^{-1}$ from the UV to visible light region and a high carrier mobility with anisotropic character. The photoelectric conversion efficiency (PCE) shows a tremendous enhancement under external strain, and shows an efficiency of up to ~16.8% at 2% compressive strain. Besides, we find that applying an external electric field can effectively modulate its band gap and band offset. Interestingly, a larger external electric field can induce nearly free electron (NFE) states around the conduction band minimum (CBM) in the GaSe/GeS heterobilayer, which leads to the band transition from a semiconductor to metallic status. These results indicate that 2D GaSe/GeS heterostructures will have widespread application prospects in future photovoltaic and optoelectric nanodevices.



## 1 Introduction

In recent decades, many two dimensional (2D) materials beyond graphene have been extensively studied, which display potential application prospects in the field of photodetectors, field-effect transistors (FETs) and spintronics, due to their distinct electronic properties.[1–4] However, it is found that no single 2D material possesses perfect properties that meet the requirements of practical applications. Recently, stacking vertically atomic thickness van der Waals (vdW) heterostructures has been confirmed to be a powerful strategy to leverage and combine the optoelectronic characteristics of different 2D materials in experiment and theory.[5–8] The 2D heterostructures, in which vdW interactions integrate different 2D materials without considering the crystal lattice mismatch, possess many tailed electronic properties that far outstripped the properties in a single component.[9] The 2D heterostructure based layered materials are considered to be good candidate materials for next-generation solar cells.[10] However, the photovoltaic efficiency of 2D heterostructure based solar cells displayed is still not ideal and needs extremely urgent improvement.

As one member of group IIIA metal monochalcogenides MX (M = Ga, In; X = S, Se, Te), the layered gallium selenide (GaSe) stacking in a Se–Ga–Ga–Se sequence has attracted growing attention due to its superior optoelectronic properties in recent years.[11,12] The GaSe crystal has a layered hexagonal structure with strong intralayer and relatively weak interlayer interactions. The monolayer GaSe can be achieved by repeatedly peeling the bulk material, which is called a micromechanical cleavage technique and it has been proven to be a convenient and efficient way to produce high quality and large size single and few layer nanosheets. So far, many optoelectronic devices based on GaSe nanosheets have been successfully fabricated.[13–17] For example, D. J. Late *et al.*[13] demonstrated the fabricated field effect transistors (FETs) based on the monolayer GaSe with ON/OFF current ratios up to $10^5$. Hu *et al.* reported that GaS nanosheet based photodetectors exhibit a superhigh photoresponsivity up to 19.2 A W$^{-1}$, which is much higher than that of graphene, $MoS_2$ and other 2D semiconductors.[14]

Additionally, germanium monochalcogenides (GeS, GeSe), which are similar to black phosphorus, have also attracted a lot

[a] Technical Center for Multifunctional Magneto-Optical Spectroscopy (Shanghai), Department of Materials, School of Physics and Electronic Science, East China Normal University, Shanghai 200241, China. E-mail: sjgong@ee.ecnu.edu.cn, zghu@ee.ecnu.edu.cn; Fax: +86-21-54342933; Tel: +86-21-54345150
[b] Key Laboratory of Polar Materials and Devices (MOE), East China Normal University, Shanghai 200241, China
[c] Collaborative Innovation Center of Extreme Optics, Shanxi University, Taiyuan, Shanxi 030006, China
[d] Shanghai Institute of Intelligent Electronics & Systems, Fudan University, Shanghai 200433, China

† Electronic supplementary information (ESI) available. See DOI: 10.1039/c9tc05840k

of research interest since their successful synthesis in experiment.[18,19] Single layer GeS has been theoretically predicted to possess a high carrier mobility ($\sim 10^3$ cm$^2$ V$^{-1}$ s$^{-1}$) with a suitable band gap value (1.65 eV), which shows promising applications in nanodevices.[20–22] It is reported that the 2D GeS monolayer has been achieved experimentally by liquid phase exfoliation recently,[23] which paves the way for fabricating the GeS based vdW heterostructure.

In this work, we construct the GaSe/GeS vdW heterostructure and investigate the combined electronic properties. Our attention was mainly focused on the band alignment, optical properties, carrier mobility and electronic field (*E*-field) effects. The results show that the GaSe/GeS heterobilayer possesses typical type-II band alignment with a direct band gap. Surprisingly, a larger external electric field can induce near free electron (NFE) states[24,25] around the conduction band minimum (CBM), which leads to the transition from a semiconductor to metallic status. The present results demonstrate that the GaSe/GeS heterobilayer may become a promising candidate material in applications of nanoelectronic devices.

## 2 Computational details

First-principles calculations were performed based on density functional theory (DFT), using the projector augmented-wave method as implemented in the Vienna *Ab initio* Simulation Package (VASP) code.[26–28] The exchange correlation functional was used within the generalized gradient approximation of Perdew, Burke and Ernzerhof.[29,30] A plane-wave basis set with a cutoff of 500 eV was used and a *k* mesh of 20 × 5 × 1 was adopted to sample the first Brillouin zone of the monolayers and heterostructure. The conjugate-gradient scheme is used for geometric optimization until the force on each atom is less than 0.01 eV Å$^{-1}$, and the total energy change is less than $10^{-5}$ eV to acquire good convergence. A sufficient vacuum space ($\geq$25 Å) is used along the *z* direction (normal to the 2D plane) to avoid periodicity interaction between adjacent images. As the van der Waals interaction cannot be effectively described by the PBE functional, the van der Waals interactions are considered by adding a semi-empirical dispersion potential to the Kohn–Sham DFT energy, through a pair-wise force field following Grimme's DFT-D2 method.[31] And optB88[32] vdW corrections are also considered for comparison. As we know, the PBE functional is known to underestimate the band gap of semiconductors. Thus, the intrinsic electronic and optical properties of the GaSe/GeS heterobilayer and the corresponding isolated monolayers are calculated using the HSE06 methods with the mixing exchange parameter of 0.25 and screening parameter of 0.2 Å$^{-1}$. The band properties of the heterostructure under an applied external electric field are calculated with the PBE methods to obtain a variation trend.

To quantitatively evaluate the relative stability of the heterostructure, the binding energy ($E_b$) of GaSe/GeS is calculated by $E_b = E_{GaSe/GeS} - (E_{GaSe} + E_{GeS})$, where $E_{GaSe/GeS}$, $E_{GaSe}$, and $E_{GeS}$ represent the total energies of the GaSe/GeS heterobilayer and GaSe and GeS monolayers, respectively.

As the absorption range of the spectrum is very important in the application of optoelectronic devices, we calculate the optical absorption coefficient by using the following formula:

$$\alpha(\omega) = \sqrt{2\omega}\left[\sqrt{\varepsilon_1(\omega)^2 + \varepsilon_2(\omega)^2} - \varepsilon_1(\omega)\right]^{1/2} \quad (1)$$

where $\varepsilon_1$ and $\varepsilon_2$ are the real part and imaginary part of the complex dielectric function, and $\varepsilon_1$ could be obtained from $\varepsilon_2$ by the Kramer–Kronig relationship. $\varepsilon_2$ is defined as:

$$\varepsilon_2(\omega) = \frac{4\pi^2 e^2}{\Omega}\lim_{q\to 0}\frac{1}{q^2}\sum_{c,v,\vec{k}} 2w_k\delta(\varepsilon_{ck} - \varepsilon_{vk} - \omega) \quad (2)$$

$$\times \langle \mu_{ck+e_\alpha}|\mu_{vk}\rangle\langle \mu_{ck+e_\beta}|\mu_{vk}{}^*\rangle \quad (3)$$

here $\alpha$ and $\beta$ represent the *x* and *y* directions, and $\Omega$ is the volume of the unit cell. The indices *c* and *v* refer to the conduction and valence band states, respectively. $\mu_{ck}$ corresponds to an eigenstate with wave vector *k*.

Furthermore, we estimated the photoelectric conversion efficiency (PCE) by using Scharber's method,[33] which is defined as follows:

$$\eta = \frac{J_{SC}V_{OC}\beta_{FF}}{P_{solar}} = \frac{0.65\left(E_g^d - \Delta E_c - 0.3\right)\int_{E_g}^{\infty}\frac{P(\hbar\omega)}{\hbar\omega}d(\hbar\omega)}{\int_0^{\infty}P(\hbar\omega)\hbar\omega} \quad (4)$$

where 0.65 is the empirical value for the band-fill factor, $E_g^d$ and $\Delta E_c$ are the donor band gap and conduction band offset, respectively. $(E_g - \Delta E_c - 0.3)$ represents the maximum open circuit voltage, and $P(\hbar\omega)$ represents the AM 1.5 solar energy flux at the value of $\hbar\omega$ for photon energy. The integral of the numerator and denominator represents the short circuit current and the incident solar irradiation, respectively. The PCE is found to be largely related to the conduction band offset ($\Delta E_c$) between the acceptor and donor materials.

To investigate the electronic transport properties of the GaSe/GeS heterobilayer, we calculated the carrier mobility based on the following expression:[34]

$$\mu_{2D} = \frac{e\hbar^3 C_{2D}}{k_B T m^* m_d E_l^2} \quad (5)$$

where $\hbar$ is the reduced Planck constant, $k_B$ is the Boltzmann constant, *T* is the temperature (300 K), $m^*$ is the obtained effective mass along the *x* and *y* directions, $m_d$ is the average effective mass defined by $\sqrt{m_x^* m_y^*}$. The $E_l$ is the deformation potential given by $E_l = \Delta E/(\Delta l/l_0)$, which denotes the shift of the band edges compared to the applied strain. $C_{2D}$ is the in-plane elastic modulus, which can be derived from the formula $(E - E_0)/S_0 = (C_{2D}/2)(\Delta l/l_0)^2$, where $E_0$ and *E* are the total energies before and after applying uniaxial strain and $S_0$ is the area of the optimized structure at the equilibrium state.

 

# 3 Results and discussion

## 3.1 Geometric structure and stability of the GaSe/GeS heterobilayer

Before studying the 2D GaSe/GeS heterobilayer model, we first investigate the GaSe and GeS monolayers. Based on the minimization of the total energy, we optimize the lattice parameters of the rectangular unit cell GaSe and GeS monolayers. For the rectangular GaSe monolayer, $a$ = 3.84 Å and $b$ = 6.65 Å, and $a$ = 3.66 Å and $b$ = 4.49 Å for the GeS unit cell (see Table 1). The band structures of the GaSe and GeS monolayers are calculated both by PBE and HSE06 functionals, which are plotted together in Fig. 1(a) and (b) for comparison. It is shown that both GaSe and GeS monolayers are indirect band gap semiconductors. The band gap value is 1.82/2.90 eV (PBE/HSE06) for the GaSe monolayer with the conduction band minimum (CBM) being located at the $\Gamma$ point and the valence band maximum (VBM) between the $\Gamma$ and $X$ points. The valence band is nearly flat in the central region of the Brillouin zone, which results in very heavy holes. For the GeS monolayer, the band gap is 1.78/2.50 eV with the CBM being located between the $\Gamma$ and $X$ points and VBM between the $\Gamma$ and $Y$ points. It is found that the shape of band structures given by two methods is very similar, in which the HSE06 result is almost a linear shift up of the PBE result in band energy. All the results are in good agreement with previous theoretical reports.[35,36]

In order to construct the GaSe/GeS vdW heterobilayer with less lattice mismatch, we construct the GaSe/GeS heterostructure

Table 1 The optimized lattice parameters $a$ and $b$ (Å) of rectangular GaSe and GeS monolayers and their band gap $E_g$ (eV) using the PBE and HSE06 methods. Some previous results are also listed for comparison

| | $a$ (Å) | $b$ (Å) | $E_g$ (PBE) (eV) | $E_g$ (HSE06) (eV) |
|---|---|---|---|---|
| GaSe | 3.84 | 6.65 | 1.82 | 2.90 |
| | 3.82[35] | 6.62[35] | 1.91[35] | 2.98[35] |
| GeS | 3.66 | 4.49 | 1.78 | 2.50 |
| | 3.68[36] | 4.40[36] | 1.65[36] | 2.32[36] |

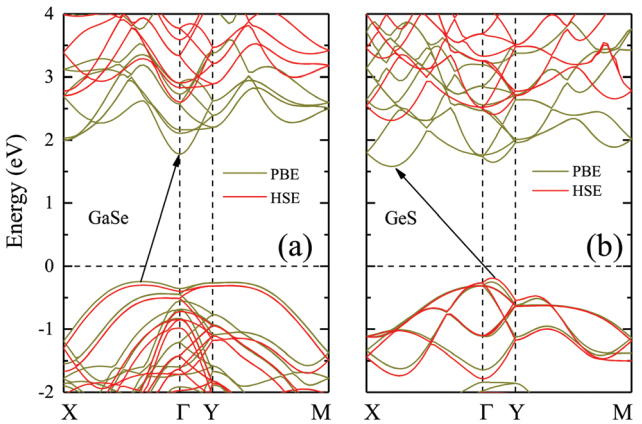


Fig. 1 The calculated band structures of monolayer GaSe and GeS are shown in (a) and (b). The blue arrows in the figure indicate the fundamental band gap, and the brown and red lines present the PBE and HSE06 results, respectively.

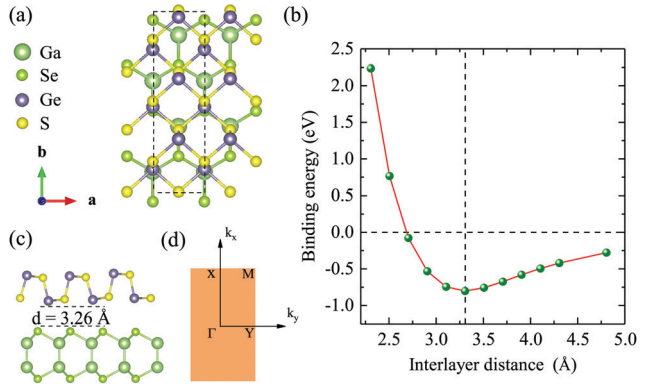


Fig. 2 (a and c) Top and side views of the GaSe/GeS heterobilayer. (b) Variation of the binding energy as a function of interlayer distances in the GaSe/GeS heterobilayer. (d) The respective Brillouin zone and the corresponding high-symmetry points $X$, $\Gamma$, $Y$, and $M$.

using a 1 × 2 × 1 GaSe rectangular supercell and a 1 × 3 × 1 GeS supercell, as shown in Fig. 2(a) and (c). The lattice mismatch along the $x$ and $y$ directions is less than 3% and 1%, respectively, which are located in a reasonable range, thus a reliable computational result can be achieved. Besides, the stacking pattern effects on the GaSe/GeS vdW heterostructures are also considered, as shown in Fig. S1 (ESI†). The results show that there is little difference in the binding energy between the different stacking configurations. The calculated band structures of two stacking patterns are very similar (see Fig. S2 in the ESI†), thus, we only take one stacking configuration as an example to study the electronic properties of GaSe/GeS heterostructures in this work. The variation of binding energy $E_b$ with the interlayer distance is shown in Fig. 2(b). The minimum binding energy for the heteobilayer is up to 0.8 eV (1.07 eV for optB88) and the equilibrium distance is calculated to be 3.26 Å. The binding energy value, which is about 60 meV per atom, has the same order of magnitude as other typical vdW heterostructures calculated within the same computational scheme (*e.g.* $MoS_2$/black phosphorus, phosphorene/graphene),[37,38] which indicates that the GaSe/GeS vdW heterostructure can be stably formed.

In Fig. 3(a) and (b), we present the projected band structure and band alignment of the GaSe/GeS vdW heterobilayer. It is found that the GaSe/GeS heterobilayer displays semiconductor characteristics with a direct band gap of 1.8 eV (HSE06), in which both the CBM and VBM lie at the $\Gamma$ point. The CBM and VBM of the GaSe layer are both lower than those of the GeS layer in energy, which forms a staggered type-II band alignment. To further confirm the type II band feature, we also calculated the band-decomposed charge density of the VBM and CBM, as shown in the inset of Fig. 3(a). The lowest-energy electron and hole states are localized on the GaSe layer and GeS layer, respectively. This indicates that the GaSe/GeS heterobilayer is a perfect type-II band alignment semiconductor, which can effectively separate the photogenerated holes and electrons. We have also performed band calculations with optB88 vdW corrections. It is found that different vdW corrections have very small effects on band dispersion and the value

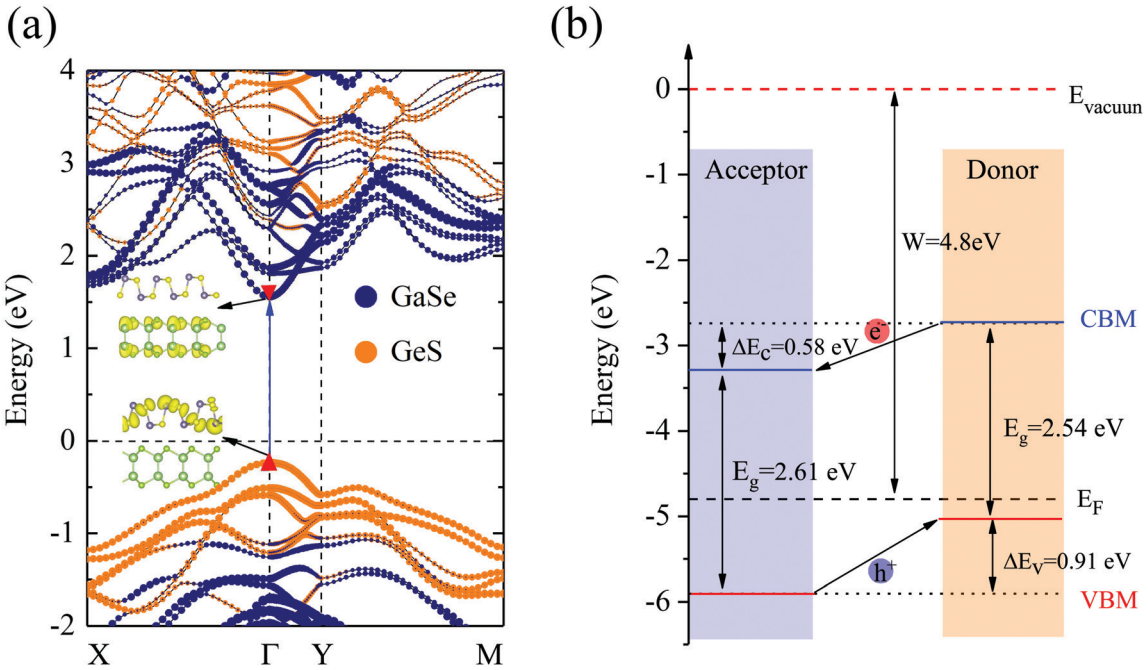


Fig. 3 (a) Projected electronic band structure of the GaSe/GeS heterobilayer calculated by using the HSE06 method. (b) Type-II donor–acceptor band alignment of the GaSe/GeS heterobilayer. The inset of (a) represents the band-decomposed charge density of the VBM and CBM for the heterostructure.

of the band gap of the heterostructure (see Fig. S3 in the ESI†). Thus, it can be a good candidate material for optoelectronic applications. In the following discussions, we will use the results from simulations with DFT-D2 corrections. Fig. 3(b) shows the band alignment of the GaSe/GeS heterobilayer, in which the vacuum level ($E_{vacuum}$) is set as a common energy reference. It is noteworthy that there is a tiny potential difference between the right (GeS) and left (GaSe) vacuum surfaces (see Fig. S4 in the ESI†). This tiny potential step is mainly caused by the dipole moment at the interface due to the charge transfer between layers. As an important factor in designing optoelectronic devices, the band offsets are presented. The valence band offset (VBO) $\Delta E_v$ and conduction band offset (CBO) $\Delta E_c$ between the GaSe and GeS layers are calculated to be about 0.91 eV and 0.58 eV, respectively. The larger band offsets can prolong the lifetime of interlayer excitons, which is crucial for improving the efficiency of carrier separation.[39] When the GaSe/GeS vdW heterobilayer is exposed to sunlight, the type-II band alignment together with the large band offset ensures the fomation of an interlayer exciton at the lowest energy in the optical spectra,[40] thus facilitating the transfer of photogenerated carriers.

The calculated optical absorption coefficient $\alpha(\omega)$ as a function of wavelength for the GaSe/GeS heterobilayer and the corresponding monolayers are shown in Fig. 4. The calculated results

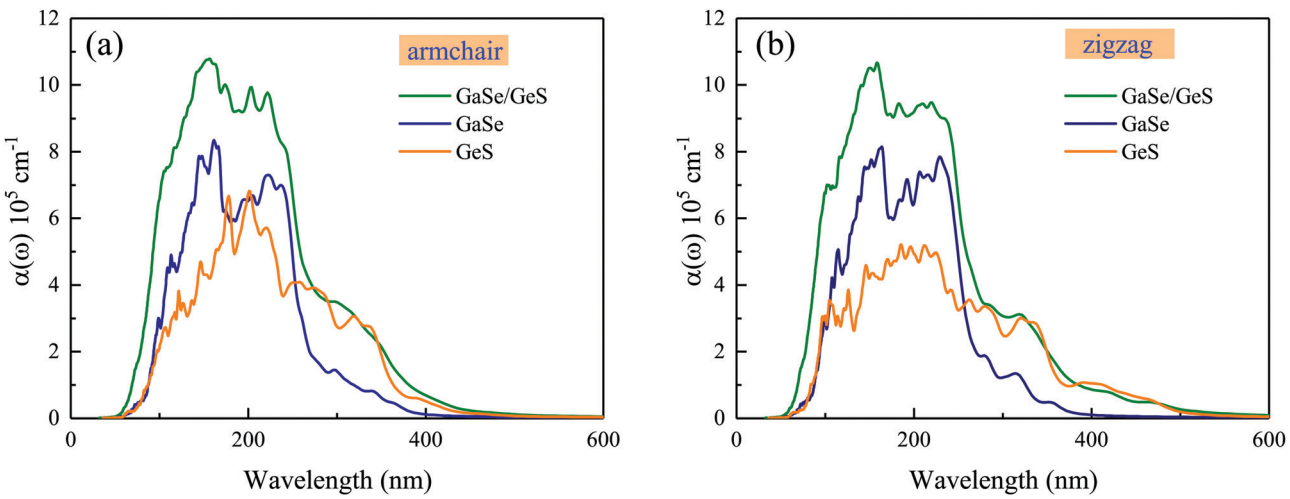


Fig. 4 The optical absorption coefficient $\alpha(\omega)$ of isolated GaSe and GeS monolayers and the GaSe/GeS heterobilayer along armchair and zigzag directions with the HSE06 method, respectively.

 

show that both the GaSe monolayer and GeS monolayer as well as the GaSe/GeS exhibit an absorption coefficient as high as $\sim 10^5$ cm$^{-1}$ from the ultraviolet light to visible light range. The optical absorption coefficient of the heterobilayer presents an obvious enhancement compared with the isolated monolayers, which suggests an enhancement of efficiency of solar energy utilization. This is mainly due to overlap of electronic states in the heterostructure caused by the charge transfer and interlayer coupling effects between two constituents.[41,42] Besides, the absorption coefficient of monolayer GeS displays anisotropic characteristics in armchair and zigzag directions, while these anisotropic characteristics are weakened in the heterobilayer.

### 3.2 Carrier mobility of the GaSe/GeS vdW heterobilayer

Based on the deformation potential theory, which is proposed by Bardeen and Shockley,[43] we calculated the carrier mobility of 2D GaSe and GeS monolayers as well as the GaSe/GeS heterobilayer at the PBE level, as it has been confirmed to be reliable for carrier mobility prediction.[44,45] The calculated carrier mobilities at room temperature (300 K) for the GaSe and GeS monolayers and their heterostructure along the $x$ and $y$ directions are listed in Table 2. The three key parameters, which determine the carrier mobility, *i.e.*, the effective mass $m^*$, deformation potential $E_l$ and the in-plane stiffness $C_{2D}$ in the propagation direction, are also listed in Table 2. The carrier mobility of 2D GeS shows anisotropic character, in which the mobilities of electrons and holes along the $x$ direction (zigzag direction) are both about 400 cm$^2$ V$^{-1}$ s$^{-1}$, while along the $y$ direction (armchair direction), the electron mobility is up to 2253 cm$^2$ V$^{-1}$ s$^{-1}$ and hole mobility is about 189 cm$^2$ V$^{-1}$ s$^{-1}$. These results are in line with the previously calculated results.[46,47] The significant difference between electron mobility and hole mobility could hinder the recombination of photogenerated carriers, thus prolonging the lifetime of carriers.[39] For the GaSe monolayer, the electron mobility is up to 583 cm$^2$ V$^{-1}$ s$^{-1}$ and 661 cm$^2$ V$^{-1}$ s$^{-1}$ along $x$ and $y$ directions, respectively. While the hole mobilities are 216 and 106 cm$^2$ V$^{-1}$ s$^{-1}$ for $x$ and $y$ directions, which are found to be close to previous results.[45] For the GaSe/GeS heterobilayer, the electron mobility is 661 cm$^2$ V$^{-1}$ s$^{-1}$ along the $x$ direction and 583 cm$^2$ V$^{-1}$ s$^{-1}$ along the $y$ direction. The hole mobility is 377 cm$^2$ V$^{-1}$ s$^{-1}$ along $x$ direction and 193 cm$^2$ V$^{-1}$ s$^{-1}$ along $y$ direction. The carrier mobilities are almost a combination of the electron mobility of GaSe and the hole mobility of GeS along the $x$ and $y$ directions. This can be attributed to the CBM and VBM of the heterostructure mainly originating from the GaSe layer and GeS layer, respectively.

### 3.3 Tunable electronic properties and enhanced photoelectric conversion efficiency (PCE) by biaxial and vertical strains

Strain engineering is an effective way to tune the electronic properties of 2D vdW heterostructures. Here, the band gap as a function of biaxial and vertical strains is presented in Fig. 5(a) and (b), in which the effective tunability of the band gap by strain engineering is clearly demonstrated. For the vertical direction, when the compressive strain is applied to the GaSe/GeS heterobilayer, in which the interlayer distance is decreased, the band gap displays a reduced trend. Conversely, when a stretch strain is exerted, a larger interlayer distance will induce an increase of the band gap. Similar behaviors can be found in GeSe/SnS heterobilayers.[48] The project band structures under different biaxial and vertical strains are presented in Fig. S5 and S6 (see the ESI†). It is noteworthy that the heterostructures retain type-II band alignment properties, independent of the biaxial and vertical strains. In Fig. 5(c), the optical absorption along the armchair and zigzag directions under biaxial strain is presented. When the strain varies from 0% to +6%, a red shift of the absorption spectrum occurred, which agree with the trend of band gap changing.

In addition, following the PCE definition mentioned in computational details, the calculated PCE of the intrinsic GaSe/GeS heterostructures is about 6.1%, which is relatively low for photovoltaic applications. According to Scharber's work, two factors are important to improve the PCE of heterostructures: one is decreasing the CBO, which can increase the $V_{oc}$, and the other is improving the $J_{sc}$ by adjusting the band gap of donors $E^d$. Both factors were involved in modulating the band structure of 2D materials in the heterostructure, which can be realized through applying external strain. The PCE contour plots of the GaSe/GeS heterostructure are shown in Fig. 5(d). It is found that the vertical and biaxial strains could greatly improve the PCE values, which facilitates solar energy utilization. The PCE reaches 11.9% when the interlayer distance decreases to 2.56 Å. While for 2% compressive strain, the PCE can reach as high as 16.8%. The power conversion efficiency is competitive with the theoretical values of many recently proposed 2D heterostructures, such as g-$SiC_2$ ($\sim$12%)[49] and $MoS_2$/phosphorene ($\sim$16%).[50] The results indicate that the high efficiency of solar energy utilization of GaSe/GeS could be realized by strain engineering, which strikingly broadens its application in optoelectric devices.

### 3.4 Electric field modulations of the electronic structures in the GaSe/GeS vdW heterobilayer

To explore the external $E$-field effects on the electronic properties of the GaSe/GeS heterobilayer, we consider the $E$-field direction

Table 2 Calculated carrier effective masses $m_x^*$, deformation potential $E_l$ (eV), in-plane stiffness $C_{2D\_x}$ (N m$^{-1}$), and mobility $\mu_x$ (cm$^2$ V$^{-1}$ s$^{-1}$) for electrons (e) and holes (h) along $x$ and $y$ directions in the GaSe/GeS heterobilayer and their corresponding individual layers at room temperature

| | Carrier type | $m_x^*/m_0$ | $m_y^*/m_0$ | $E_{lx}$ | $E_{ly}$ | $C_{2D\_x}$ | $C_{2D\_y}$ | $\mu_x$ | $\mu_y$ |
|---|---|---|---|---|---|---|---|---|---|
| GaSe | Electron | 0.24 | 0.17 | 8.29 | 9.40 | 84.88 | 74.62 | 472.30 | 525.48 |
| | Hole | 1.33 | 2.08 | 1.94 | 2.07 | 84.88 | 74.62 | 216.11 | 106.70 |
| GeS | Electron | 0.53 | 0.38 | 3.04 | 1.60 | 46.63 | 14.61 | 426.44 | 2253.51 |
| | Hole | 0.25 | 0.27 | 6.00 | 4.82 | 46.63 | 14.61 | 421.58 | 189.52 |
| GaSe/GeS | Electron | 0.39 | 0.18 | 6.35 | 8.39 | 130.38 | 89.47 | 661.89 | 583.54 |
| | Hole | 0.64 | 0.76 | 4.04 | 4.29 | 130.38 | 89.47 | 377.22 | 193.30 |

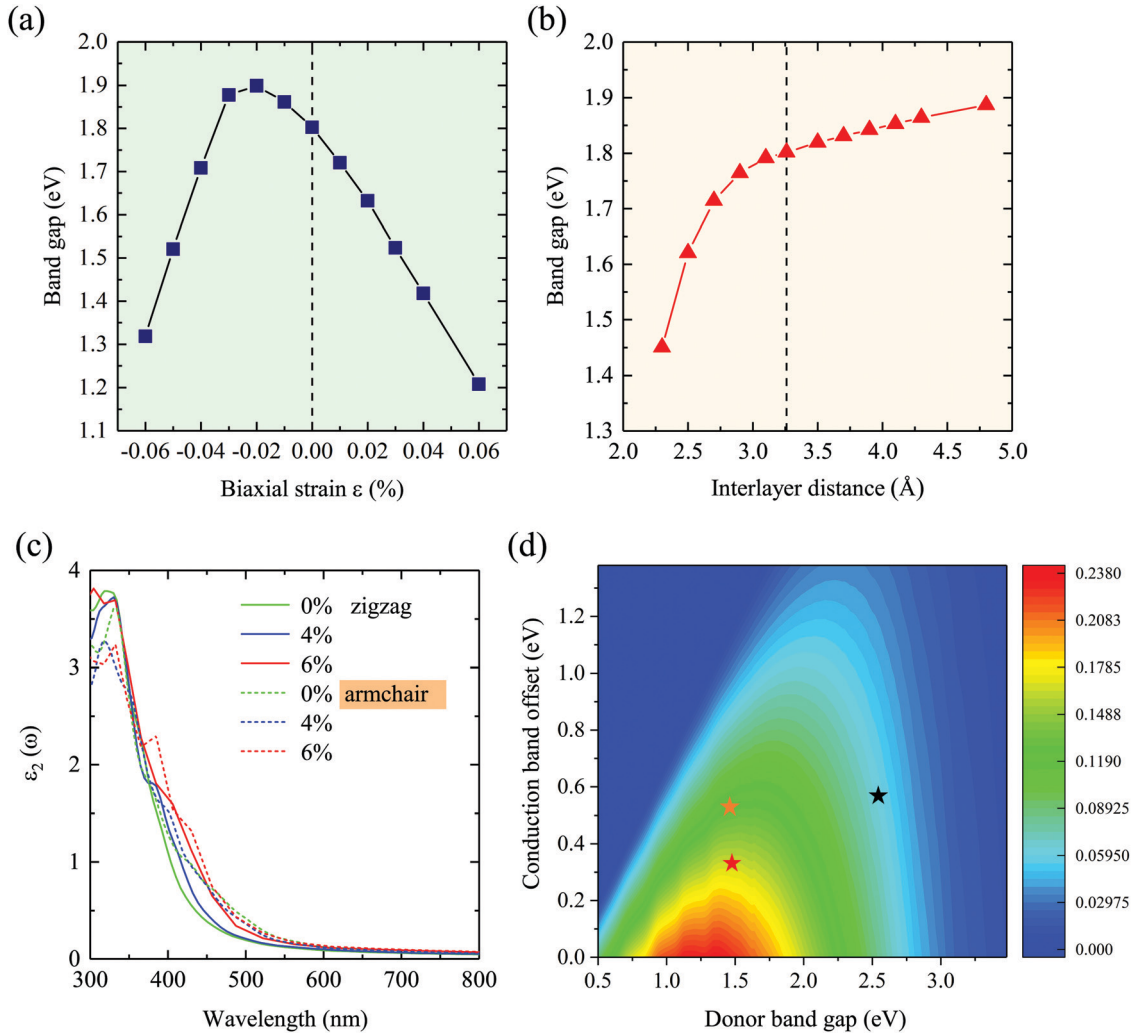


Fig. 5 (a and b) Calculated band gap of the GaSe/GeS heterobialayer under different biaxial and vertical strain by the HSE06 functional. (c) The frequency-dependent imaginary dielectric function $\varepsilon_2(\omega)$ along zigzag and armchair directions under different biaxial tensile strains. (d) Contour plot of power conversion efficiency (%) of the GaSe/GeS heterostructure. The dark, orange and red stars represent the GaSe/GeS heterobilayer at no strain, vertical strain ($d_{int}$ = 2.59 Å), and compressive strain (at 2%), respectively.

perpendicular to GaSe/GeS. The positive direction of the *E*-field is defined as pointing from the GeS layer to the GaSe layer. The projected band structures of the GaSe/GeS heterobilayer with several selected external *E*-fields are shown in Fig. 6. The GaSe/GeS retains type-II band alignment characteristics under the *E*-field of $-0.8$ V Å$^{-1}$ to 0.6 V Å$^{-1}$. Interestingly, it is found that extra conduction bands appear near the CBM in the heterostructure, when the applied *E*-field increases over to $E_c$ = 0.6 V Å$^{-1}$ ($-0.8$ V Å$^{-1}$ for the negative *E*-field). This phenomenon can be attributed to the electric field induced near free electron (NFE) states in the heterostructure.[24,25] The NFE states are not contributed by any electrons around GaSe or GeS layers. The energy level of the NFE bands drops down quickly upon increasing the amplitude of the external *E*-field. When the applied electric field reaches 0.8 V Å$^{-1}$ ($-0.9$ V Å$^{-1}$), the rapid decline of NFE bands can induce the metallic conducting band structure feature of the GaSe/GeS heterobilayer.

The band gap as a function of the external *E*-field for the GaSe/GeS heterobilayer is shown in Fig. 7(a). Our results show that the band gap can be modulated effectively through the external electric field, which rely on both the intensity and direction of the *E*-field. When the positive *E*-field is applied, the band gap increases first, and then starts to decrease rapidly when the *E*-field strength is beyond 0.6 V Å$^{-1}$. While the negative *E*-field is applied, the band gap displays a monotonously decreasing trend. The band gap exhibits a linear modulation effect within $E_c$ ($-0.8$ V Å$^{-1}$, 0.6 V Å$^{-1}$). The band gap is closed when the intensity of the positive (negative) *E*-field is larger than 0.8($-0.9$) V Å$^{-1}$. Besides, we shift the zero-gap for the hybrid functional according to the band gap differences between PBE and HSE06.[25] Thus, the band gap can extend a variety of fitting lines to the HSE06 zero-gap range. The band offsets of the GaSe/GeS heterobilayer that varied with the external *E*-field are also plotted in Fig. 7(a). We see that both the values of $\Delta E_v$ and $\Delta E_c$ exhibit a continuously decreasing trend with the applied *E*-field changing from $-0.8$ V Å$^{-1}$ to 0.6 V Å$^{-1}$. In Fig. 7(b), we show the evolution of band edges under the external *E*-field. It can be seen that as the *E*-field is varied from $-0.8$ to 0.6 V Å$^{-1}$, the CBM and VBM of

 

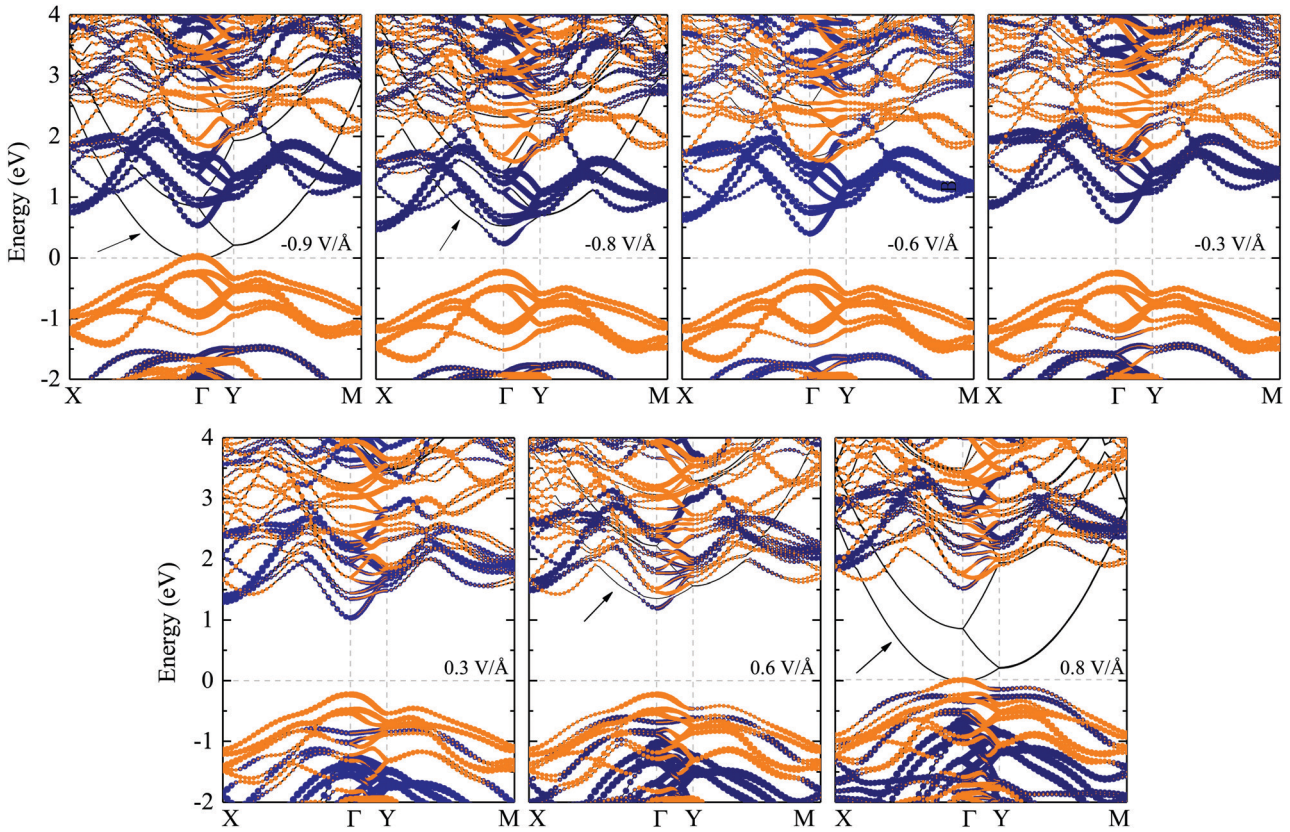


Fig. 6 The projected electronic band structures of the GaSe/GeS heterobilayer with different selected electric fields. The dark blue and orange dots represent the results from GaSe and GeS, respectively. Note that the black arrows denote the NFE states.

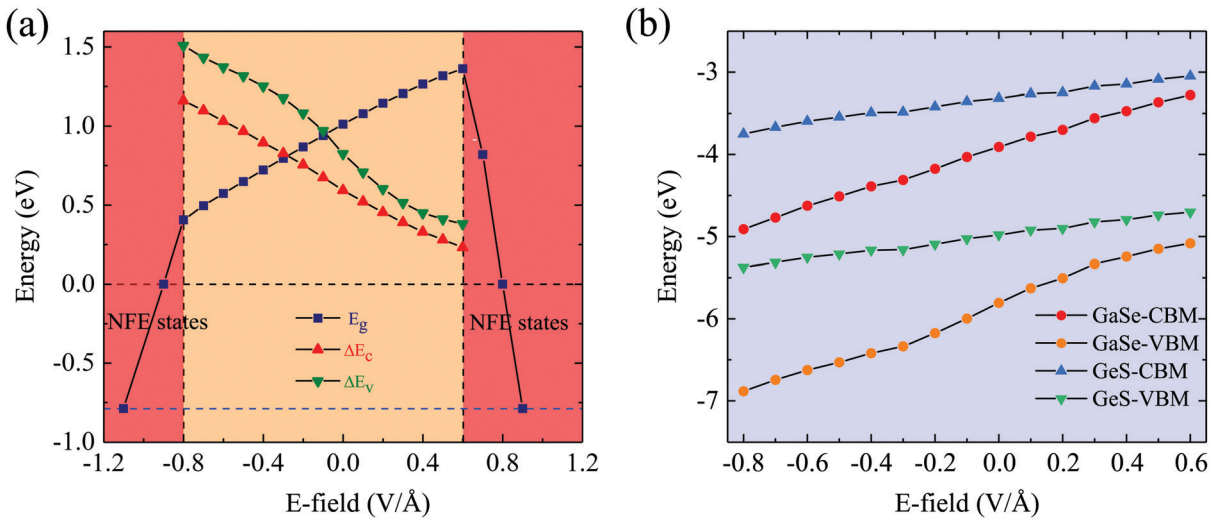


Fig. 7 (a) Evolution diagram of the band gap and band offsets of the GaSe/GeS heterobilayer as a function of the electric field. (b) Evolution of the band edges of GaSe and GeS in the GaSe/GeS heterobilayer as a function of the electric field. Note that the blue dash line in figure (a) means the shifted zero-gap for the hybrid functional according to the band gap differences between the PBE and HSE06 methods.

the GaSe layer move upward, while the band edges of the GeS monolayer change little. As the energy of band edges for GeS is always higher than that for the GaSe layer, the heterostructure retains type-II band alignment features in the range of $-0.8$ V Å$^{-1}$ to 0.6 V Å$^{-1}$ for the external $E$-field. In addition, the GaSe/GeS heterobilayer retains direct band gap features, which is in favour of light absorption. When the applied external electric field reaches $-0.8$ V Å$^{-1}$, the band gap decreases to about 1.1 eV (HSE06 level), which is suitable for application in optical absorption within the visible region.

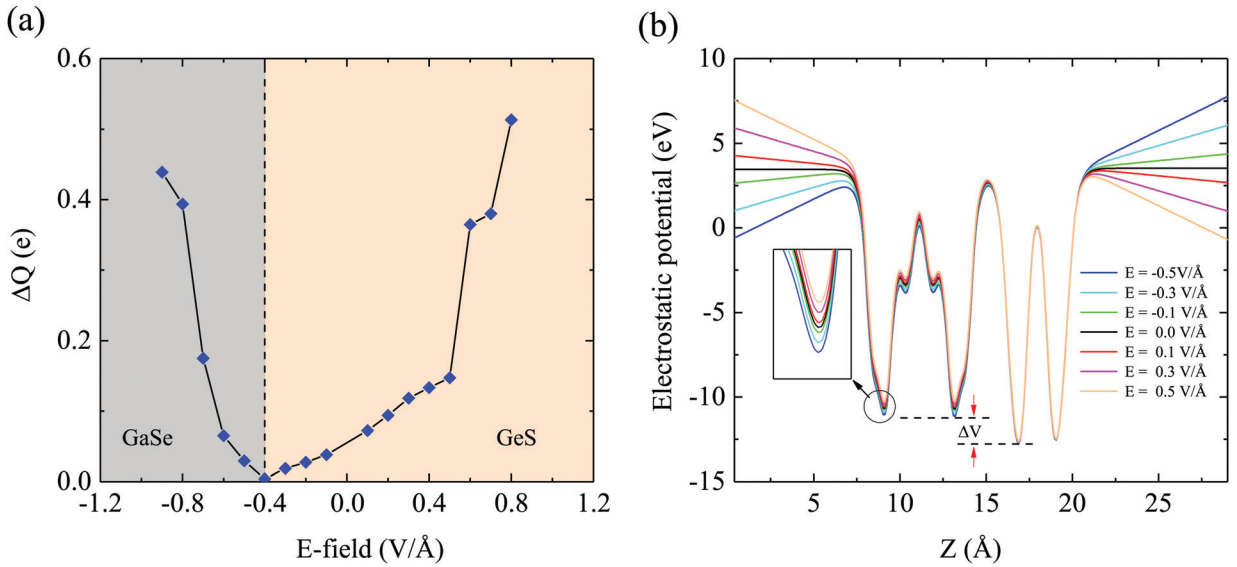


Fig. 8 (a) Charge transfer as a function of the external electric field in the GaSe/GeS heterostructure. (b) Electrostatic potentials of GaSe/GeS with different applied electric fields.

To understand the physical mechanism of charge transfer between GaSe and GeS monolayers under the *E*-field, we performed the Bader charge analysis.[51] The number of transferred electrons between the two layers as a function of the external *E*-field is shown in Fig. 8(a). When the external *E*-field is 0 V Å$^{-1}$, we find that there are net electrons being transferred from the GaSe to GeS layer, and this can be attributed to the built-in *E*-field along with the direction of the positive external electric field induced by a larger electrostatic potential drop between two layers.[52] When the negative *E*-field is applied gradually, the electrons that are transferred from the GaSe to GeS layer start to decrease, which is due to the reduced net effective internal electric field crossing the interface. When the strength of the external *E*-field reaches −0.4 V Å$^{-1}$, the net charges transferred between the two layers are almost zero. As the negative *E*-field is further increased, the electrons start to transfer from the GeS to GaSe layer. Meanwhile, we also calculate the electrostatic potentials of GaSe/GeS under an external electric field, as shown in Fig. 8(b). With the external electric field increasing from negative to postive, the potential well of GaSe rises up notably, leading to a larger interfacial electrostatic potential difference Δ*V*. Thus, a stronger interfacial electrostatic field forms, which leads to more charge transfer between GaSe and GeS layers. All the results indicate that the GaSe/GeS heterostructure can be used as a good candidate for next generation optoelectronic devices.

## 4 Conclusions

In summary, by using first-principles calculations, we reveal that the 2D GaSe/GeS vdW heterobilayer is a robust type-II band alignment semiconductor with a direct band gap of 1.8 eV. The heterobilayer shows an excellent absorbance coefficient of ~$10^5$ cm$^{-1}$ from the UV to visible light range. Meanwhile, the GaSe/GeS heterobilayer possesses a high carrier mobility and displays anisotropic character. The calculated photoelectric conversion efficiency displays a tremendous enhancement under applied external strain, and shows as high as 16.8% at 2% compressive strain. The band gap and band offset of the GaSe/GeS heterobilayer can be effectively modulated through applying a vertical electric field. Moreover, we also find that the GaSe/GeS heterostructure can be transformed into its NFE states under a large electric field. We believe that the theoretical results will shed light on the design and application of novel two-dimensional material-based photovoltaic electronic devices in the future.

## Conflicts of interest

There are no conflicts to declare.

## Acknowledgements

The authors would like to thank Dr Wenzhen Dou from Beihang University for constructive discussions. This work was financially supported by the National Natural Science Foundation of China (Grant No. 91833303, 61774058, 61974043, and 61674057), and the National Key R&D Program of China (Grant No. 2017YFA0303403 and 2018YFB0406500), the Projects of Science and Technology Commission of Shanghai Municipality (Grant No. 18JC1412400, 18YF1407200, 18YF1407000, and 19511120100), and the Program for Professor of Special Appointment (Eastern Scholar) at Shanghai Institutions of Higher Learning.

## References

1 S. Z. Butler, S. M. Hollen, L. Cao, Y. Cui, J. A. Gupta, H. R. Gutierrez, T. F. Heinz, S. S. Hong, J. Huang, A. F. Ismach, E. Johnston-Halperin, M. Kuno, V. V. Plashnitsa, R. D. Robinson,

 

R. S. Ruoff, S. Salahuddin, J. Shan, L. Shi, M. G. Spencer, M. Terrones, W. Windl and J. E. Goldberger, *ACS Nano*, 2013, **7**, 2898–2926.
2 G. R. Bhimanapati, Z. Lin, V. Meunier, Y. Jung, J. Cha, S. Das, D. Xiao, Y. Son, M. S. Strano, V. R. Cooper, L. Liang, S. G. Louie, E. Ringe, W. Zhou, S. S. Kim, R. R. Naik, B. G. Sumpter, H. Terrones, F. Xia, Y. Wang, J. Zhu, D. Akinwande, N. Alem, J. A. Schuller, R. E. Schaak, M. Terrones and J. A. Robinson, *ACS Nano*, 2015, **9**, 11509–11539.
3 S. J. Gong, C. Gong, Y. Y. Sun, W. Y. Tong, C. G. Duan, J. H. Chu and X. Zhang, *Proc. Natl. Acad. Sci. U. S. A.*, 2018, **115**, 8511–8516.
4 L. P. Xu, P. Zhang, H. Jiang, X. Wang, F. F. Chen, Z. G. Hu, Y. J. Gong, L. Y. Shang, J. J. Zhang, K. Jiang and J. H. Chu, *Small*, 2019, 1904116.
5 A. K. Geim and I. V. J. N. Grigorieva, *Nature*, 2013, **499**, 419.
6 K. S. Novoselov, A. Mishchenko, A. Carvalho and A. H. Castro Neto, *Science*, 2016, **353**, aac9439.
7 C. Gong and X. Zhang, *Science*, 2019, **363**, 706.
8 F. Withers, O. Del Pozo-Zamudio, A. Mishchenko, A. P. Rooney, A. Gholinia, K. Watanabe, T. Taniguchi, S. J. Haigh, A. K. Geim, A. I. Tartakovskii and K. S. Novoselov, *Nat. Mater.*, 2015, **14**, 301–306.
9 X. Wang and F. Xia, *Nat. Mater.*, 2015, **14**, 264–265.
10 Q. Xiang, J. Yu and M. Jaroniec, *J. Am. Chem. Soc.*, 2012, **15**, 6575–6578.
11 W. Feng, W. Zheng, W. W. Cao and P. A. Hu, *Adv. Mater.*, 2014, **26**, 6587–6593.
12 W. Huang, L. Gan, H. Li, Y. Ma and T. Zhai, *CrystEngComm*, 2016, **18**, 3968–3984.
13 D. J. Late, B. Liu, J. Luo, A. Yan, H. S. Matte, M. Grayson, C. N. Rao and V. P. Dravid, *Adv. Mater.*, 2012, **24**, 3549–3554.
14 P. Hu, L. Wang, M. Yoon, J. Zhang, W. Feng, X. Wang, Z. Wen, J. C. Idrobo, Y. Miyamoto, D. B. Geohegan and K. Xiao, *Nano Lett.*, 2013, **13**, 1649–1654.
15 H. Huang, P. Wang, Y. Gao, X. Wang, T. Lin, J. Wang, L. Liao, J. Sun, X. Meng, Z. Huang, X. Chen and J. Chu, *Appl. Phys. Lett.*, 2015, **107**, 143112.
16 P. Hu, Z. Wen, L. Wang, P. Tan and K. Xiao, *ACS Nano*, 2012, **6**, 5988–5994.
17 X. Li, M. W. Lin, J. Lin, B. Huang, A. A. Puretzky, C. Ma, K. Wang, W. Zhou, S. T. Pantelides, M. Chi, I. Kravchenko, J. Fowlkes, C. M. Rouleau, D. B. Geohegan and K. Xiao, *Sci. Adv.*, 2016, **2**, e1501882.
18 D. D. Vaughn, R. J. Patel, M. A. Hickner and R. E. Schaak, *J. Am. Chem. Soc.*, 2010, **132**, 15170–15172.
19 C. Li, L. Huang, G. P. Snigdha, Y. Yu and L. Cao, *ACS Nano*, 2012, **6**, 8868–8877.
20 F. Li, X. Liu, Y. Wang and Y. Li, *J. Mater. Chem. C*, 2016, **4**, 2155–2159.
21 X. Lv, W. Wei, Q. Sun, F. Li, B. Huang and Y. Dai, *Appl. Catal., B*, 2017, **217**, 275–284.
22 S. Zhang, N. Wang, S. Liu, S. Huang, W. Zhou, B. Cai, M. Xie, Q. Yang, X. Chen and H. Zeng, *Nanotechnology*, 2016, **27**, 274001.
23 D. Lam, K. S. Chen, J. Kang, X. L. Liu and M. C. Hersam, *Chem. Mater.*, 2018, **30**, 2245–2250.
24 M. Khazaei, A. Ranjbar, M. Ghorbani-Asl, M. Arai, T. Sasaki, Y. Liang and S. Yunoki, *Phys. Rev. B: Condens. Matter Mater. Phys.*, 2016, **93**, 205125.
25 X. Yang, B. Sa, H. Zhan and Z. Sun, *J. Mater. Chem. C*, 2017, **5**, 12228–12234.
26 P. E. Blöchl, *Phys. Rev. B: Condens. Matter Mater. Phys.*, 1994, **50**, 17953–17979.
27 G. Kresse and J. Hafne, *Phys. Rev. B: Condens. Matter Mater. Phys.*, 1993, **47**, 558.
28 G. Kresse and J. Hafne, *Phys. Rev. B: Condens. Matter Mater. Phys.*, 1994, **49**, 14251.
29 J. P. Perdew, K. Burke and M. Ernzerhof, *Phys. Rev. Lett.*, 1996, **77**, 3865.
30 T. Kerber, M. Sierka and J. Sauer, *J. Comput. Chem.*, 2008, **29**, 2088–2097.
31 S. Grimme, *J. Comput. Chem.*, 2006, **27**, 1787–1799.
32 A. D. Becke, *Phys. Rev. B: Condens. Matter Mater. Phys.*, 1988, **38**, 3098.
33 M. C. Scharber, D. Muhlbacher, M. Koppe, P. Denk, C. Waldauf, A. J. Heeger and C. Brabec, *Adv. Mater.*, 2010, **20**, 579–583.
34 J. Qiao, X. Kong, Z. X. Hu, F. Yang and W. Ji, *Nat. Commun.*, 2014, **5**, 4475.
35 H. L. Zhuang and R. G. Hennig, *Chem. Mater.*, 2013, **25**, 3232–3238.
36 L. C. Gomes and A. Carvalho, *Phys. Rev. B: Condens. Matter Mater. Phys.*, 2015, **92**, 085406.
37 K. Tang, W. Qi, Y. Li and T. Wang, *J. Phys. Chem. C*, 2018, **122**, 7027–7032.
38 Y. Cai, G. Zhang and Y.-W. Zhang, *J. Phys. Chem. C*, 2015, **119**, 13929–13936.
39 M. Palummo, M. Bernardi and J. C. Grossman, *Nano Lett.*, 2015, **15**, 2794–2800.
40 E. Torun, H. P. C. Miranda, A. Molina-Sĺćnchez and L. Wirtz, *Phys. Rev. B: Condens. Matter Mater. Phys.*, 2018, **97**, 245427.
41 X. H. Niu, Y. H. Li, H. B. Shu, X. J. Yao and J. L. Wang, *J. Phys. Chem. C*, 2017, **121**, 3648.
42 J. M. Liao, B. S. Sa, J. Zhou, R. Ahuja and Z. M. Sun, *J. Phys. Chem. C*, 2014, **118**, 17594.
43 J. Bardeen and W. Shockley, *Phys. Rev.*, 1950, **80**, 72–80.
44 Y. Q. Cai, G. Zhang and Y. W. Zhang, *J. Am. Chem. Soc.*, 2014, **136**, 6269–6275.
45 Y. Cui, L. Peng, L. Sun, Q. Qian and Y. Huang, *J. Mater. Chem. A*, 2018, **6**, 22768–22777.
46 X. Lv, W. Wei, Q. Sun, F. Li, B. Huang and Y. Dai, *Appl. Catal., B*, 2017, **217**, 275–284.
47 L. Xu, M. Yang, S. J. Wang and Y. P. Feng, *Phys. Rev. B: Condens. Matter Mater. Phys.*, 2017, **95**, 235434.
48 C. Xia, J. Du, W. Xiong, Y. Jia, Z. Wei and J. Li, *J. Mater. Chem. A*, 2017, **5**, 13400–13410.
49 L. J. Zhou, Y. F. Zhang and L. M. Wu, *Nano Lett.*, 2013, **13**, 5431–5436.
50 J. Dai and X. C. Zeng, *J. Phys. Chem. Lett.*, 2014, **5**, 1289–1293.
51 G. Henkelman, A. Arnaldsson and H. Jonsson, *Comput. Mater. Sci.*, 2006, **36**, 354–360.
52 Y. C. Rao, S. Yu and X. M. Duan, *Phys. Chem. Chem. Phys.*, 2017, **19**, 17250–17255.